Monthly Notices
of the
ROYAL ASTRONOMICAL SOCIETY
MNRAS **456,** 2707–2716 (2016) doi:10.1093/mnras/stv2861

# A clean sightline to quiescence: multiwavelength observations of the high Galactic latitude black hole X-ray binary Swift J1357.2−0933

Richard M. Plotkin,[1,2★] Elena Gallo,[1] Peter G. Jonker,[3,4] James C. A. Miller-Jones,[2] Jeroen Homan,[5] Teo Muñoz-Darias,[6,7] Sera Markoff,[8] Montserrat Armas Padilla,[6,7] Rob Fender,[9] Anthony P. Rushton,[9,10] David M. Russell[11] and Manuel A. P. Torres[3,4,12]

[1]*Department of Astronomy, University of Michigan, 1085 South University Ave, Ann Arbor, MI 48109, USA*
[2]*International Centre for Radio Astronomy Research, Curtin University, GPO Box U1987, Perth, WA 6845, Australia*
[3]*SRON, Netherlands Institute for Space Research, Sorbonnelaan 2, NL-3584 CA Utrecht, the Netherlands*
[4]*Department of Astrophysics/IMAPP, Radboud University Nijmegen, Heyendaalseweg 135, NL-6525 AJ Nijmegen, the Netherlands*
[5]*Kavli Institute for Astrophysics and Space Research, Massachusetts Institute of Technology, 70 Vassar Street, Cambridge, MA 02139, USA*
[6]*Instituto de Astrofsica de Canarias, E-38205 La Laguna, Tenerife, Spain*
[7]*Departamento de Astrofsica, Univ. de La Laguna, E-38206 La Laguna, Tenerife, Spain*
[8]*Anton Pannekoek Institute for Astronomy, University of Amsterdam, Science Park 904, NL-1098 XH Amsterdam, the Netherlands*
[9]*Department of Physics, Astrophysics, University of Oxford, Keble Road, Oxford OX1 3RH, UK*
[10]*School of Physics and Astronomy, University of Southampton, Highfield, Southampton SO17 1BJ, UK*
[11]*New York University Abu Dhabi, PO Box 129188, Abu Dhabi, United Arab Emirates*
[12]*European Southern Observatory, Alonso de Córdova 3107, Vitacura, Casilla 19001, Santiago de Chile, Chile*

Accepted 2015 December 4. Received 2015 December 3; in original form 2015 August 27

## ABSTRACT

We present coordinated multiwavelength observations of the high Galactic latitude ($b = +50^\circ$) black hole X-ray binary (BHXB) Swift J1357.2−0933 in quiescence. Our broad-band spectrum includes strictly simultaneous radio and X-ray observations, and near-infrared, optical, and ultraviolet data taken 1–2 d later. We detect Swift J1357.2−0933 at all wavebands except for the radio ($f_{5\,\mathrm{GHz}} < 3.9\,\mu\mathrm{Jy\ beam^{-1}}$; $3\sigma_{\mathrm{rms}}$). Given current constraints on the distance (2.3–6.3 kpc), its 0.5–10 keV X-ray flux corresponds to an Eddington ratio $L_{\mathrm{X}}/L_{\mathrm{Edd}} = 4 \times 10^{-9}$–$3 \times 10^{-8}$ (assuming a black hole mass of $10\,\mathrm{M}_\odot$). The broad-band spectrum is dominated by synchrotron radiation from a relativistic population of outflowing thermal electrons, which we argue to be a common signature of short-period quiescent BHXBs. Furthermore, we identify the frequency where the synchrotron radiation transitions from optically thick-to-thin ($\nu_{\mathrm{b}} \approx$ 2–5 $\times\ 10^{14}$ Hz), which is the most robust determination of a 'jet break' for a quiescent BHXB to date. Our interpretation relies on the presence of steep curvature in the ultraviolet spectrum, a frequency window made observable by the low amount of interstellar absorption along the line of sight. High Galactic latitude systems like Swift J1357.2−0933 with clean ultraviolet sightlines are crucial for understanding black hole accretion at low luminosities.

**Key words:** accretion, accretion discs – stars: individual: Swift J1357.2−0933 – ISM: jets and outflows – X-rays: binaries.

## 1 INTRODUCTION

Black hole X-ray binaries (BHXBs) in the hard X-ray spectral state (see Remillard & McClintock 2006 for a review) are nearly always associated with compact radio emission from a steady state relativistic jet (e.g. Hjellming & Johnston 1988; Fender 2001). Correlated radio and X-ray variability on day- to week-long time-scales implies a coupling between the relativistic outflow and the underlying accretion flow (e.g. Heinz & Sunyaev 2003; Markoff et al. 2003; Gallo, Miller & Fender 2012; Corbel et al. 2013; Gallo et al. 2014). The radio emission arises from partially self-absorbed synchrotron radiation from the compact jet (Blandford & Königl 1979). Meanwhile, X-ray emission includes contributions from a radiatively inefficient accretion flow (RIAF; e.g. Ichimaru 1977; Narayan & Yi 1994; Abramowicz et al. 1995; Blandford & Begelman 1999; Narayan, Igumenshchev & Abramowicz 2000; Quataert & Gruzinov 2000; Yuan, Cui & Narayan 2005) and optically thin synchrotron radiation from the jet (e.g. Markoff, Falcke & Fender 2001; Markoff et al. 2003; Russell et al. 2010, 2013; Plotkin et al. 2012). A cool inner

★E-mail: richard.plotkin@curtin.edu.au

disc may also contribute X-ray emission (Miller et al. 2006; Reis, Fabian & Miller 2010).

A substantial number of hard state BHXBs have been discovered to be radio underluminous at a given X-ray luminosity, when compared to more 'traditional' systems (e.g. Corbel et al. 2004; Jonker et al. 2004; Brocksopp et al. 2005; Cadolle Bel et al. 2007; Rodriguez et al. 2007; Xue & Cui 2007; Coriat et al. 2011; Soleri & Fender 2011; Gallo et al. 2012; Cao, Wu & Dong 2014; Meyer-Hofmeister & Meyer 2014). It is not clear, however, whether this diversity in radio properties continues after BHXBs transition into the quiescent spectral state (Eddington ratios[1] $L_{\rm X}/L_{\rm Edd} \lesssim 10^{-5}$; Plotkin, Gallo & Jonker 2013). In fact, at least three 'radio underluminous' systems have been observed to transition to the 'traditional' radio/X-ray luminosity correlation[2] around $L_{\rm X}/L_{\rm Edd} \lesssim 10^{-4\,-\,5}$ (e.g. H1743−322, Jonker et al. 2010; Coriat et al. 2011; XTE J1752−223, Ratti et al. 2012; MAXI J1659−152, Jonker et al. 2012), perhaps hinting that the 'radio underluminous' BHXB branch does not extend indefinitely towards the lowest X-ray luminosities.

Our currently limited knowledge on quiescent BHXB accretion flows/jets stems primarily from their low luminosities levels, combined with the small number of known BHXBs located close to the Earth (e.g. Calvelo et al. 2010; Miller-Jones et al. 2011). There are currently only three low-mass BHXB systems (with a confirmed black hole accretor) that have meaningful, *simultaneous* radio and X-ray constraints on their jets in quiescence, V404 Cyg ($L_{\rm X}/L_{\rm Edd} \approx 10^{-6}$; Hjellming et al. 2000; Gallo, Fender & Hynes 2005; Hynes et al. 2009), A0620−00 ($L_{\rm X}/L_{\rm Edd} \approx 10^{-8.5}$; Gallo et al. 2006), and XTE J1118+480 ($L_{\rm X}/L_{\rm Edd} \approx 10^{-8.5}$; Gallo et al. 2014). The (high-mass) Be/black hole X-ray binary system MWC 656 also has non-simultaneous radio and X-ray detections in quiescence ($L_{\rm X}/L_{\rm Edd} \approx 10^{-8}$; Munar-Adrover et al. 2014; Dzib, Massi & Jaron 2015). Multiwavelength constraints on more systems are needed to understand the disc/jet connection in quiescence.

Here, we present new coordinated radio, near-infrared (NIR), optical, ultraviolet (UV), and X-ray observations of the BHXB Swift J1357.2−0933 (hereafter J1357.2) in quiescence. In Section 2, we provide a brief overview of the properties of J1357.2. This source displayed unusual behaviour in the hard state (Corral-Santana et al. 2013), and Section 2 is intended to help put the current work into context. In Section 3 we describe our multiwavelength observations, and results are presented in Section 4. In Section 5 we describe a serendipitous discovery of the 2011 outburst from archival infrared data. Finally, our results are discussed in Section 6, and our main conclusions are highlighted in Section 7. Error bars are quoted at the 68 per cent confidence level, unless stated otherwise. We adopt a distance ranging from 2.3 to 6.3 kpc (Shahbaz et al. 2013; Mata Sánchez et al. 2015), an orbital inclination angle $i > 70^\circ$ (Corral-Santana et al. 2013; Torres et al. 2015), and we assume a black hole mass of $10\,{\rm M}_\odot$ (Mata Sánchez et al. 2015).

## 2 SWIFT J1357.2−0933

J1357.2 was discovered by the *Swift* Burst Array Telescope (BAT) on 2011 January 28 (Krimm et al. 2011a). The distance is not well determined, and we adopt a range of $2.3 < d < 6.3$ kpc here. The lower limit is based on disc veiling constraints from optical spectroscopy in quiescence (Mata Sánchez et al. 2015); the upper limit arises from an estimate of the degree to which synchrotron radiation could be diluting starlight from the companion, given the orbital period and inclination of the system (Shahbaz et al. 2013). If the distance happens to fall towards the lower end, then J1357.2 would be the least-luminous known BHXB in quiescence (Armas Padilla et al. 2014b), and it would be one of the few known BHXBs suitable for deep radio observations to search for a quiescent radio jet. Furthermore, J1357.2 has a high Galactic latitude ($b = +50^\circ$), making it one of the few known BHXBs with a low-enough Galactic absorption column density to allow UV studies in quiescence (XTE J1118+480 is another notable BHXB at high Galactic latitude; see McClintock et al. 2003).

From time-resolved optical spectroscopy of broad, double-peaked H$\alpha$ emission in outburst, Corral-Santana et al. (2013) found an orbital period of $2.8 \pm 0.3$ h, and Mata Sánchez et al. (2015) recently constrained the black hole mass to be $>9.3\,{\rm M}_\odot$. Corral-Santana et al. (2013) also discovered recurring dips in the outburst optical light curve on 2–8 min time-scales, where the flux dropped by up to ∼0.8 mag. They explain this remarkable short-term variability as J1357.2 being viewed at a nearly edge-on inclination angle ($i \gtrsim 70^\circ$), with the dipping behaviour being caused by a geometrically thick obscuring torus in the inner disc. From time-resolved spectroscopy of the quiescent optical counterpart, Torres et al. (2015) also favour a high orbital inclination, based on the profiles of broad, double-peaked H$\alpha$. The proposed geometrically thick inner toroidal structure could be a crucial component of all accretion flows (and potentially important for producing and sustaining jets), but its signatures cannot be detected in other systems at lower inclination angles.

The odd optical 'dipping' behaviour observed during outburst persists into quiescence, albeit at longer recurring time-scales of ∼30 m (Shahbaz et al. 2013). Intriguingly, Shahbaz et al. (2013) find that, superposed on the dips, there is stochastic, large-amplitude optical/NIR variability (the fractional optical rms is ≈35 per cent). This variability is highlighted by 10–30 m flare events with amplitudes up to 1.5–2 mag. Because of this variability, as well as a steep NIR/optical spectrum ($f_\nu \propto \nu^{-1.4}$), Shahbaz et al. (2013) argue that the NIR/optical spectrum is dominated by synchrotron radiation emitted by a thermal jet.

## 3 OBSERVATIONS AND DATA REDUCTION

We targeted J1357.2 through a joint *Chandra*–National Radio Astronomy Observatory (NRAO) program (ObsID 15782; PI: Plotkin), with simultaneous *Chandra* and Very Large Array (VLA) observations taken on 2014 March 20 (see Section 3.1). We also obtained quasi-simultaneous NIR, optical, and UV observations, which were taken 1–2 d after the radio/X-ray data (see Section 3.2). The full spectral energy distribution (SED) is summarized in Table 1.

### 3.1 Strictly simultaneous observations

#### *3.1.1 Radio observations*

The radio observations were taken with the Karl G. Jansky VLA on 2014 March 20, from 04:20 to 14:18 UT under project code SF0459. The array was in its most-extended A-configuration. We observed in two 1024-MHz basebands, with central frequencies of 4.8 and 5.8 GHz. The data were processed using the Common

[1] The Eddington luminosity for hydrogen in a spherical geometry is $L_{\rm Edd} = 1.26 \times 10^{38} (M/{\rm M}_\odot)\ {\rm erg\,s^{-1}}$, where $M$ is the black hole mass.
[2] We (somewhat arbitrarily) call BHXBs that follow radio/X-ray luminosity correlations of the form $L_{\rm r} \propto L_{\rm X}^{\approx 0.6}$ as 'traditional' here for historical reasons (e.g. Gallo, Fender & Corbel 2003).

**Table 1.** Observing log and SED.

| Telescope | Date[a] | Filter | Exposure time (ks) | Frequency (Hz) | Flux dens.[b] (μJy) |
|---|---|---|---|---|---|
| VLA | 2014 March 20 UT 04:20 | *C* band | 30.5 | $5.30 \times 10^9$ | <4.2 |
| VLA[c] | 2013 July 9–11 + 2014 March 20 | *C* band | 46.2 | $5.30 \times 10^9$ | <3.9 |
| WHT | 2014 March 20–21 | $K_s$ | 5 | $1.39 \times 10^{14}$ | $32.2 \pm 1.6$ |
| WHT | ... | *H* | 5 | $1.80 \times 10^{14}$ | $30.6 \pm 1.3$ |
| WHT | ... | *J* | 4.5 | $2.43 \times 10^{14}$ | $29.8 \pm 1.0$ |
| LT | 2014 March 21–22 | $i'$ | 1.4 | $4.01 \times 10^{14}$ | $28.4 \pm 1.0$ |
| LT | ... | $r'$ | 1.6 | $4.86 \times 10^{14}$ | $22.7 \pm 1.0$ |
| *Swift* | 2014 March 21 | *u* | 1.7 | $8.65 \times 10^{14}$ | $12.4 \pm 1.8$ |
| *Swift* | ... | *uvw1* | 1.7 | $1.15 \times 10^{15}$ | $3.1 \pm 1.0$ |
| *Swift* | ... | *uvm2* | 1.7 | $1.33 \times 10^{15}$ | <2.1 |
| *Chandra* | 2014 March 20 UT 02:40 | ACIS-S3 | 25.5 | 0.5–10 keV | $(8.2 \pm 1.9) \times 10^{-15}$[d] |

*Notes.* [a]The universal time (UT) is listed for the beginning of the simultaneous radio and X-ray observations. For the NIR and optical observations, data were taken by cycling through each filter over each observing night. The *Swift* observations were taken by cycling through each UVOT filter (with 60–360 s exposures), beginning at UT 07:40.
[b]Flux densities are reported after applying corrections for interstellar extinction, as described in Section 3.2. See the text for values prior to applying extinction corrections. Upper limits are quoted at the $3\sigma$ level, and all error bars are at the 68 per cent level. Upper limits for VLA radio observations have units μJy beam$^{-1}$.
[c]Throughout the text, we adopt the more sensitive radio upper limit obtained when combining the 2014 radio observation with two archival VLA observations from 2013 (see Section 3.1.1).
[d]Unabsorbed flux from 0.5 to 10 keV in erg s$^{-1}$ cm$^{-2}$, assuming $\Gamma = 2.1$ and no intrinsic absorption.

Astronomy Software Application (CASA; McMullin et al. 2007). We used 3C 286 to set the amplitude scale according to the Perley & Butler (2013) coefficients within CASA's SETJY task, and we used the extragalactic calibrator source J1408-0752 to determine the complex gain solutions in the direction of the target. Our on-source time was 508 min. Following external gain calibration, we made an image of the field surrounding J1357.2, using two Taylor terms to model the frequency dependence of the sources in the field and thereby avoid amplitude errors in the deconvolution. We used Briggs weighting with a robust value of 1 as the best compromise between achieving high sensitivity and downweighting the sidelobes of the dirty beam. We placed outlier fields on known bright sources outside the main image, to ensure that their sidelobes did not affect the final image. We do not detect J1357.2 to a $3\sigma$ upper limit of 4.2 μJy beam$^{-1}$.

In an attempt to place a deeper radio flux density limit, we also retrieved two archival VLA observations taken under project code 13A-203 (PI: Fender), which added 261 min on-source. The two archival observations were taken on 2013 July 9–10 (23:13-01:57 UT) and 10–11 (23:24–02:08 UT), when the array was in the more compact C-configuration. The observing set-up and calibration sources were identical to our 2014 observation. We calibrated the two archival data sets separately, and we combined all three epochs of VLA data into a single image. When creating the combined image, we accounted for the mismatch in angular scales probed by the two array configurations by using the multiscale clean algorithm implemented in CASA's CLEAN task, and we tried different data weighting schemes. Our best image was made by removing the shortest baselines (<10 kλ) and using a robust weighting of 1. J1357.2 is not detected in the combined image, with a $3\sigma$ upper limit of 3.9 μJy beam$^{-1}$. We adopt this more sensitive <3.9 μJy beam$^{-1}$ limit throughout the text, which corresponds to a radio luminosity $L_r < 1.3 \times 10^{26}$–$9.8 \times 10^{26}$ erg s$^{-1}$ at 5.3 GHz, assuming a flat radio spectrum and $2.3 < d < 6.3$ kpc.

#### 3.1.2 X-ray

The *Chandra* observations were taken on 2014 March 20 UT 02:40–10:40. J1357.2 was placed at the aim point of the S3 chip on the Advanced CCD Imaging Spectrometer (ACIS; Garmire et al. 2003). Data were telemetered in very faint mode, which we then reprocessed with the *Chandra* Interactive Analysis of Observations (CIAO) software (Fruscione et al. 2006), applying the latest calibration files (CALDB 4.6.5). We removed 200 s from the exposure, during which there was a slightly elevated sky level, yielding an effective exposure time of 25.5 ks. The remaining analysis was performed over 0.5–7 keV. Photometry was performed over a circular aperture with a 10-pixel radius, centred at the optical/NIR position from Rau, Greiner & Filgas (2011). The background was estimated over a circular annulus with inner and outer radii of 20 and 40 pixels, respectively. We obtained 21 total counts, with an estimated 1.5 background counts in the circular aperture, yielding a net count rate of $(0.8 \pm 0.2) \times 10^{-3}$ counts s$^{-1}$. We use the Interactive Spectral Interpretation System (ISIS; Houck & Denicola 2000) to calculate an unabsorbed 0.5–10 keV model flux of $f_X = (8.2 \pm 1.9) \times 10^{-15}$ erg s$^{-1}$ cm$^{-2}$, assuming an unabsorbed power law[3] with $\Gamma = 2.1$ (see Section 4.1). For distances 2.3–6.3 kpc, our 2014 *Chandra* flux corresponds to 0.5–10 keV luminosities $5.2 \times 10^{30}$–$3.9 \times 10^{31}$ erg s$^{-1}$ and $L_X/L_{Edd} = 4.1 \times 10^{-9}$–$3.1 \times 10^{-8}$ (assuming $M_{BH} = 10\,M_\odot$).

### 3.2 Quasi-simultaneous observations

Observations at other wavebands were taken 1–2 d after the simultaneous radio VLA and *Chandra* X-ray observations. All magnitudes and flux densities in the following text are reported prior to correcting for Galactic extinction; all data in figures and in Table 1 are

[3] $N_E = N_0(E/E_0)^{-\Gamma}$, where $\Gamma$ is the X-ray photon index, $N_E$ is the photon flux density at energy $E$, and $N_0$ is the normalization at energy $E_0 = 1$ keV.

presented after correcting for extinction, assuming $A_V = 0.123$ and $E(B-V) = 0.04$ in the optical/UV (as adopted by Armas Padilla et al. 2013; Shahbaz et al. 2013). For UV observations with the *Swift* Ultraviolet/Optical Telescope (UVOT; Roming et al. 2005) (see Section 3.2.3), we adopt the $A_\lambda/A_V$ ratios tabulated by Kataoka et al. (2008) for each UVOT filter.

#### 3.2.1 Near-infrared

NIR observations were taken on the night starting 2014 March 20 (PI: Jonker), using the Long-slit Intermediate Resolution Infrared Spectrometer (LIRIS) on the 4.2-m William Herschel Telescope (WHT). We cycled through the $J, H$, and $K_s$ filters over the night. Seeing conditions were generally poor, approximately 1.25 arcsec (full width at half-maximum) in the $K_s$ band. For the first sequence in the $J$ filter, we applied a five-point dither pattern, taking five exposures of 20 s each per dither position. Once we visually confirmed that J1357.2 was detected in that sequence, we switched to a 10-point dither pattern for all filters (with $5 \times 20$ s exposures per position). We cycled through five dither sequences per filter over the night, exposing for a total of 4500 s in the $J$ filter, and 5000 s in $H$ and $K_s$.

Sky subtraction and flat-fielding were performed using routines from the LIRIS data reduction pipeline THELI (Schirmer 2013). Individual frames were then combined to create a single image in each filter. J1357.2 was detected in all three filters. We performed differential photometry, calibrated to two nearby (unsaturated) stars detected in the Two Micron All Sky Survey (2MASS; Skrutskie et al. 2006). We find $J = 19.32 \pm 0.03$, $H = 18.81 \pm 0.04$, and $K_s = 18.29 \pm 0.05$ mag (on the 2MASS magnitude scale), with the uncertainties dominated by the error in the 2MASS photometric zero-points.

We searched for intranight NIR variability by co-adding the exposures from each individual dither sequence, which resulted in five time-resolved images per filter. Each time-resolved image represents 1000 s of exposure time, except for the first $J$-band image which includes 500 s. We do not detect any obvious short-term variability that is significantly larger than the uncertainty on each flux measurement: the magnitudes in each sliced $J$, $H$, and $K_s$ image vary by $\pm 0.16$, 0.14, and 0.06 mag, respectively, but uncertainties on each magnitude measurement are typically comparable, with $\sigma_m \approx \pm 0.13$, 0.09, and 0.10 mag, respectively, in each filter. We are likely not sensitive to the short-term NIR variability observed by Shahbaz et al. (2013), given the cadence and length of our NIR exposures.

#### 3.2.2 Optical

We observed J1357.2 in the optical on the night starting 2014 March 21 (PI: Fender) with the IO:O camera on the 2-m Liverpool Telescope (LT) on La Palma, Spain (Steele et al. 2004). We alternated between the $r'$ and $i'$ filters, taking a total of $18 \times 200$ s exposures in each filter. Observations were carried out under much variable weather and seeing conditions, especially during the first half of the run. For this reason we only consider the last eight exposures taken in each band for our analysis (one additional $i'$ exposure was excluded because of a cosmic ray).

Data were bias subtracted and flat-field corrected using standard procedures in IRAF. Photometry was calibrated to nearby stars in the Sloan Digital Sky Survey (SDSS) catalogue. We find $r'$ and $i'$ in the range $20.4 \pm 0.1$–$20.9 \pm 0.2$ and $20.1 \pm 0.1$–$20.7 \pm 0.2$ mag, respectively, consistent with the optical variability on minute-long time-scales reported by Corral-Santana et al. (2013) and Shahbaz et al. (2013). In order to increase signal-to-noise ratio (and to average over the short-term variability), the individual exposures were combined to produce a single image per filter. This yields $r' = 20.62 \pm 0.05$ mag and $i' = 20.35 \pm 0.04$ mag after 1600 and 1400 s on target, respectively.

#### 3.2.3 Ultraviolet

UV observations were taken with *Swift*/UVOT on 2014 March 21 07:40 (PI: Homan). Data were taken by cycling through the *u*, *uvw1*, and *uvm2* filters (1700 s exposures in each filter). Individual frames were combined using the UVOTIMSUM tool. Flux densities were obtained with the UVOTSOURCE tool, using circular source and background extraction regions with 4 and 11.5 arcsec radii, respectively. J1357.2 was detected in the *u* and *uvw1* filters, with flux densities of $10.3 \pm 1.8$ (*u*) and $2.40 \pm 0.98$ μJy (*uvw1*). J1357.2 was not detected in the *uvm2* filter, with a flux density $<1.63$ μJy ($3\sigma$ limit).

## 4 RESULTS

### 4.1 X-ray spectrum

We extracted an X-ray spectrum using the CIAO tool SPECEXTRACT. Given the low-number of X-ray counts, we only attempted to fit a POWER-LAW model to the spectrum. We perform the spectral fitting within ISIS, using Cash statistics (Cash 1979) with the background included in the fit (an energy-dependent aperture correction was applied to account for the finite size of the extraction region). We initially fixed the column density to the Galactic value of $N_H = 1.2 \times 10^{20}$ cm$^{-2}$ (Krimm, Kennea & Holland 2011b; Armas Padilla et al. 2014b), and we found a best-fitting photon index $\Gamma = 2.6 \pm 0.9$. Armas Padilla et al. (2014a) found negligible X-ray absorption for J1357.2 from a high-count *XMM–Newton* X-ray spectrum taken during its 2011 outburst. Indeed, when we refit the quiescent *Chandra* X-ray spectrum allowing $N_H$ to vary as a free parameter, $N_H$ converges towards zero and the best-fitting photon index remains similar ($\Gamma = 2.6^{+1.2}_{-0.8}$). This photon index is consistent with an *XMM–Newton* observation in quiescence taken by Armas Padilla et al. (2014b) in 2013 July, who found a best-fitting $\Gamma = 2.1 \pm 0.4$, and it is typical of other quiescent BHXB systems ($\Gamma \sim 2.1$; Plotkin et al. 2013; Reynolds et al. 2014). To ease comparison to Armas Padilla et al. (2014b), we adopt the canonical $\Gamma = 2.1$ and no column density for flux and luminosity calculations, unless stated otherwise.[4]

### 4.2 Multiwavelength correlations

#### 4.2.1 Radio/X-ray

In Fig. 1 we show J1357.2 in the radio/X-ray luminosity plane, with luminosities illustrated from 2.3 to 6.3 kpc. Even considering the distance uncertainty, our ($3\sigma$) radio limit on J1357.2 in quiescence

[4] Adopting $\Gamma = 2.6$ and $N_H = 1.2 \times 10^{20}$ cm$^{-2}$ provides an unabsorbed 0.5–10 keV model flux $f_x = (7.1 \pm 2.1) \times 10^{-15}$ erg s$^{-1}$ cm$^{-2}$, which is similar within the errors to the $f_X = (8.2 \pm 1.9) \times 10^{-15}$ erg s$^{-1}$ cm$^{-2}$ reported in Section 3.1.2 when adopting $\Gamma = 2.1$ and no absorption. The difference in luminosity between the two spectral fits is therefore negligible compared to the uncertainty on the distance.

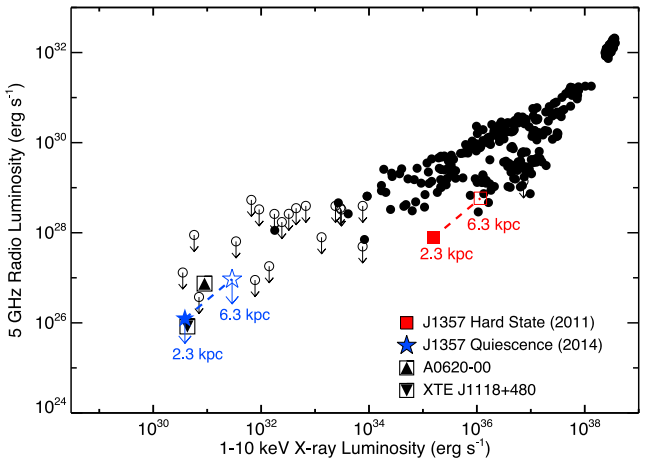


**Figure 1.** J1357.2 in the radio/X-ray luminosity plane, including our observations in quiescence (blue star symbols) and nearly simultaneous hard-state observations from the literature (red squares). The luminosity range due to the unknown distance of J1357.2 is illustrated by dashed lines connected to filled (2.3 kpc) and open (6.3 kpc) symbols. Data points for other BHXBs are taken from Gallo et al. (2014), where filled circles denote radio detections, and open circles/arrows denote radio non-detections. The locations of A0620−00 and XTE J1118+480 in quiescence are highlighted in the figure (see legend; both BHXBs have radio detections at $L_{\rm X}/L_{\rm Edd} \approx 10^{-8.5}$).

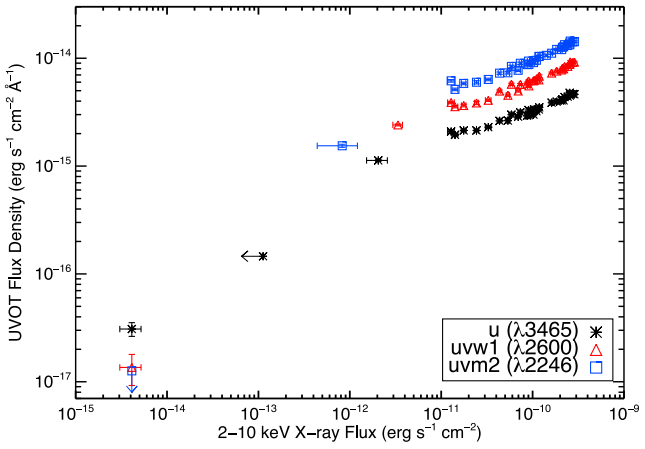


**Figure 2.** The UV/X-ray luminosity correlation for J1357.2. The UV filters (from *Swift*/UVOT) and their effective wavelengths are noted in the legend. Hard state data are taken from Armas Padilla et al. (2013) during the 2011 outburst decay (we only include filters for which we have quiescent observations), and the data points at the lowest X-ray flux are from our recent campaign in quiescence. The shape of the UV spectrum changes in quiescence and becomes redder (i.e. steeper).

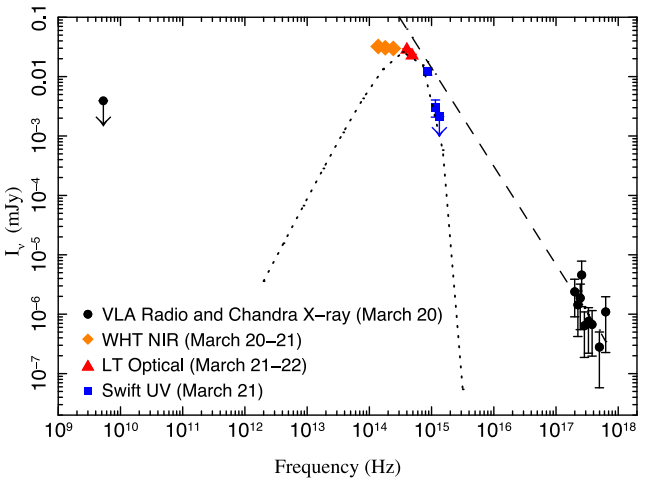


**Figure 3.** Broad-band quiescent spectrum of J1357.2 from our quasi-simultaneous multiwavelength campaign in 2014 March. Data points are coded by date of observation (see legend for details). *Chandra* data are unfolded, binned to >2 counts per bin. We also show our best-fitting X-ray power-law spectrum ($\Gamma = 2.6$; dashed line) extrapolated to lower frequencies, and a blackbody curve ($T_{\rm bb} = 7000 \pm 300$ K) that fits the optical/UV data (dotted line). We illustrate the X-ray spectrum with the best-fitting $\Gamma = 2.6$ instead of the canonical $\Gamma = 2.1$ adopted elsewhere in the paper, in order to more conservatively illustrate that the UV spectrum is steeper than the X-ray spectrum.

(blue stars) indicates that its $L_{\rm r}/L_{\rm X}$ ratio is not any larger than A0620−00. Near the peak of the 2011 outburst, a radio counterpart was detected from J1357.2 in the hard state on 2011 February 4, with a flux density of 245 ± 54 μJy (Sivakoff, Miller-Jones & Krimm 2011). We combine that radio flux density with a hard-state *XMM–Newton* observation taken on 2011 February 5 (red square; Armas Padilla et al. 2014a, unabsorbed $f_{0.5-10\,{\rm keV}} = 3.3 \times 10^{-10}$ erg s$^{-1}$ cm$^{-2}$). Regardless of the distance, it is clear from Fig. 1 that J1357.2 fell on the 'radio underluminous' branch of the $L_{\rm r}$–$L_{\rm X}$ diagram in the hard state. Our new VLA observation in quiescence is therefore the most sensitive radio constraint on a BHXB known to be radio faint in the hard state, although it is unclear if J1357.2 remained radio underluminous in quiescence, or if it transitioned to the 'traditional' radio/X-ray correlation.

#### 4.2.2 *UV/X-ray*

J1357.2 is only the second BHXB with quasi-simultaneous UV and X-ray detections deep in quiescence (after XTE J1118+480; McClintock et al. 2003; Plotkin et al. 2015). Only J1357.2 also has simultaneous high-cadence UV and X-ray monitoring observations during the outburst decay (Armas Padilla et al. 2013). The decay UV/X-ray correlation from Armas Padilla et al. (2013) is shown in Fig. 2, along with our new data point in quiescence. It is clear that the UV/X-ray correlation does not extend unbroken into quiescence. Instead, the slope steepens between the final hard state monitoring observations and our new quiescent epoch. Interestingly, the shape of the UV spectrum also appears to have changed: in the hard state, the flux is brightest in the *uvm2* filter, fainter in the *uvw1* filter, and faintest in the *u* filter; the opposite is observed in quiescence.

### 4.3 Broad-band spectrum

The quiescent broad-band spectrum is shown in Fig. 3, where it can be seen that the NIR, optical, and UV spectra become increasingly steeper. The NIR spectrum is consistent with being flat (i.e. $f_\nu \propto$ constant): from our $K_{\rm s}$ and *J*-band observations, we measure a NIR spectral index $\alpha_{\rm nir} = -0.1 \pm 0.1$ ($f_\nu \propto \nu^\alpha$). Our optical $r'$ and $i'$ observations (which were taken on the same observing night) follow a steeper spectrum, $\alpha_{\rm opt} = -1.2 \pm 0.3$, which is consistent with the steep spectrum seen at earlier epochs (Shahbaz et al. 2013 found $f_\nu \propto \nu^{-1.4}$). Our *Swift*/UVOT observations indicate that the spectrum becomes even steeper at the highest observed UV energies ($\alpha_{\rm uv} < -2.6$ between the *uvw1* and *uvm2* filters).

Given the change in spectral index between the NIR and UV bands, we attempt to fit the NIR–UV spectrum with a single

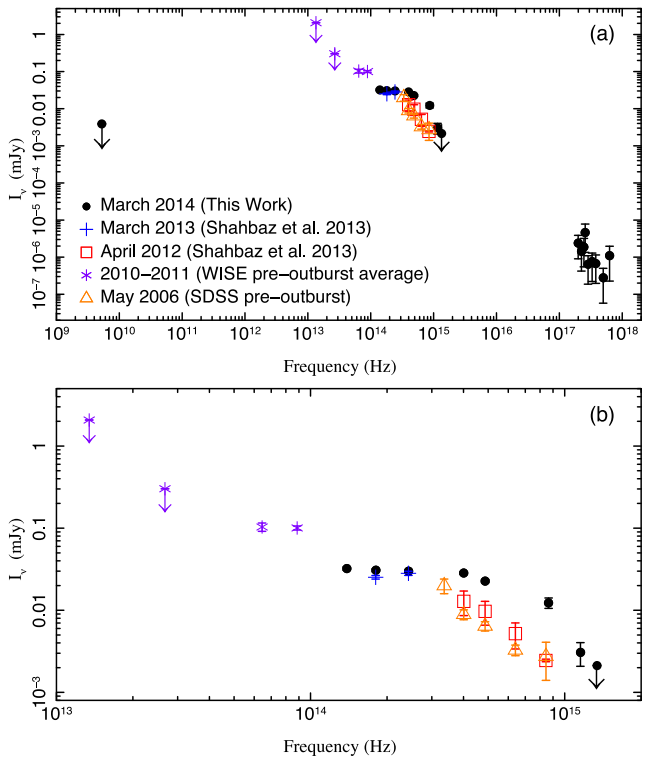


**Figure 4.** Broad-band spectrum of J1357.2 with archival IR, NIR, and optical observations. Black circles are data from our 2014 quiescent campaign (repeated from Fig. 3). Other symbols denote NIR and optical data at previous epochs (as published by Shahbaz et al. 2013), pre-outburst optical data from the SDSS, and pre-outburst IR observations from *WISE* (see legend for details). For clarity, panel (b) shows a zoom-in of the IR–UV portion of the spectrum.

temperature blackbody, but all fits are poor and underpedict the NIR flux. We next explore the possibility that a single temperature blackbody explains only the optical–UV radiation, and we find $T_{\rm bb} = 7000 \pm 300$ K from a least-squares fit (Markwardt 2009). Since there is likely day-long variability between the quasi-simultaneous optical and UV epochs, we do not expect to obtain a reduced $\chi^2_{\rm r} \approx 1$ during the fit (i.e. our statistical error bars underestimate the uncertainty because they neglect systematic errors; see e.g. Markoff et al. 2015). To derive the uncertainty on the best-fitting $T_{\rm bb}$, we therefore adopt an empirical scheme where we fix the blackbody normalization to the best-fitting value and calculate blackbody curves for a grid of temperatures centred on 7000 K. For the 99.7 per cent (i.e. $3\sigma$) confidence interval, we adopt the range of temperatures that produce blackbody curves that pass through the $\pm 3\sigma$ error limits of at least one (detected) optical–UV data point, which corresponds to $6100 < T_{\rm bb} < 7900$ K (i.e. $\sigma_{T_{\rm bb}} = \pm 300$ K). In all cases, if the optical–UV emission were to be blackbody radiation from a cool accretion disc, then an extra emission component would be necessary to also explain the NIR spectrum (see Fig. 3). We suggest in Section 6.1 that synchrotron radiation can alternatively explain the entire NIR–UV spectrum, without any need to include additional components.

### 4.4 Flux variability

In Fig. 4 we compare our 2014 broad-band spectrum to previous IR through optical observations in quiescence. These archival observations include pre-outburst data of the optical counterpart from the SDSS (2006), and post-outburst NIR and optical quiescent observations from 2012–2013 taken by Shahbaz et al. (2013). We only incorporate archival data with exposures >20 min in at least two filters on the same observing night, in order to retain some simultaneous spectral information, and to average over short-term variability at a level comparable to our 2014 campaign (our shortest 2014 observation was 23 min). We also include in Fig. 4 (pre-outburst) IR observations from the *Wide-field Infrared Survey Explorer* (*WISE*; Wright et al. 2010).

J1357.2 is a factor of 2–5 brighter at all frequencies during our 2014 campaign except for the NIR. The *Chandra* X-ray flux is almost a factor of 3 brighter than the quiescent flux from an *XMM–Newton* observation obtained 9 months earlier (Armas Padilla et al. 2014b find $f_{\rm X} = 3.2 \times 10^{-15}$ erg s$^{-1}$ cm$^{-2}$, compared to $f_{\rm X} = 8.2 \times 10^{-15}$ erg s$^{-1}$ cm$^{-2}$ from *Chandra*). This level of X-ray variability is typical for quiescent BHXB systems (e.g. Hynes et al. 2004; Bernardini & Cackett 2014). On the same day as the *XMM–Newton* observation, a fainter optical flux of $r' = 22.29 \pm 0.08$ mag (omitted from Fig. 4 for clarity) was observed with the LT (Armas Padilla et al. 2014b); our 2014 $r'$ flux measurement is 4–5 times brighter. Our other optical LT and UVOT $u$ flux measurements are also brighter by a similar factor. Interestingly, the NIR data points do *not* display the same level of long-term variability (and the 2014 NIR data also appear to follow a relatively flat spectrum). However, no epochs besides our 2014 campaign have coordinated NIR and optical data, so it is possible that the previous NIR observations were also taken when the source was relatively bright. The apparently elevated *WISE* IR flux densities are discussed in Section 5.

## 5 ARCHIVAL PRE-OUTBURST INFRARED OBSERVATIONS

*WISE* took IR observations on three separate epochs, covering 2010 January, 2010 July, and 2011 January (we take flux densities directly from the *ALLWISE*[5] data release; we note that the *WISE* constraints on J1357.2 presented by Shahbaz et al. 2013 only include data from the 2010 January epoch, which were the only publicly available data at the time). Flux densities from co-added images of all three *WISE* epochs appear consistent with a flat IR spectrum (Fig. 4), albeit at a higher flux density compared to the flat NIR spectrum that we observed in 2014.

Serendipitously, the final *WISE* observations were taken on 2011 January 20, only 8 d before J1357.2 was discovered in outburst in the X-ray. We show IR light curves in the *WISE W1* (3.4 μm) and *W2* (4.6 μm) filters in Fig. 5 (the longer wavelength *WISE* filter channels were not operational during the 2011 epoch), and the 2011 IR flux density is clearly elevated compared to the earlier 2010 *WISE* epochs. Many of the *WISE* IR magnitudes are lower limits, so in order to quantify differences in IR fluxes between *WISE* epochs, we use the Astronomy Survival Analysis (ASURV) package rev 1.2 (Lavalley, Isobe & Feigelson 1992), which implements the statistical methods presented in Feigelson & Nelson (1985). In the following, we compare the 2011 January epoch (12 data points in each filter) to all 2010 epochs (22 data points in the *W1* filter, and 12 data points in the *W2* filter).[6] The IR magnitudes are brighter during 2011: incorporating the lower limits, the mean

[5] http://wise2.ipac.caltech.edu/docs/release/allwise/

[6] We combine both 2010 epochs here to improve the statistics, because we do not see evidence that the distributions of *WISE* magnitudes are different between 2010 January and 2010 July. A Peto–Prentence test indicates that

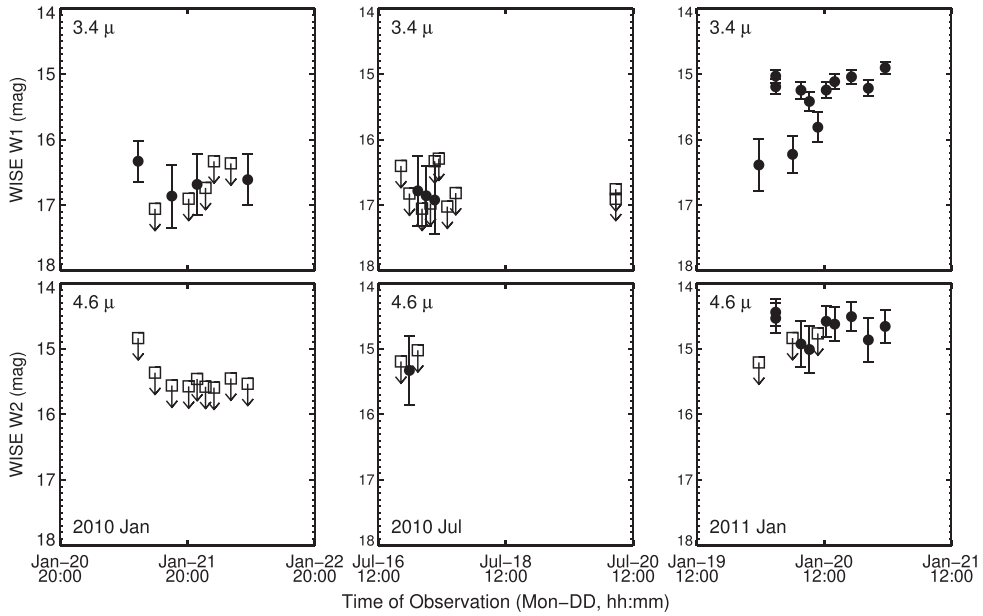


**Figure 5.** Pre-outburst IR light curves of J1357.2 in the *WISE W1* (top row) and *W2* (bottom row) filters. Observations taken during 2010 January, 2010 July, and 2011 January are shown in the left-hand, middle, and right-hand columns, respectively. Filled circles with error bars illustrate detections, while open squares represent 95 per cent lower limits on the magnitude. The 2011 January observations were taken only 8 d before J1357.2 was discovered in outburst in the X-ray, indicating that the outburst rise time-scale was $\lesssim$1 week.

magnitudes on 2011 January 20 are $\langle W_1 \rangle = 15.40 \pm 0.13$ mag and $\langle W_2 \rangle = 14.78 \pm 0.073$ mag, compared to $\langle W_1 \rangle = 16.90 \pm 0.047$ mag and $\langle W_2 \rangle = 15.56 \pm 0.027$ mag during 2010. Furthermore, a Peto–Prentence test indicates that the *WISE* magnitudes in 2011 versus 2010 are unlikely drawn from the same parent distributions ($p < 10^{-4}$ for both the *W1* and *W2* filters).

The elevated IR flux during the 2011 *WISE* epoch might represent the early stages of the outburst. However, since the 2011 IR light curve does not monotonically increase with time, we cannot exclude the possibility that the enhanced IR flux is a result of typical levels of variability expected in quiescence. Regardless, the fact that J1357.2 was still so faint in the IR only 8 d before the X-ray outburst discovery (which occurred when J1357.2 was already close to the peak of the X-ray outburst; Krimm et al. 2011a) is consistent with expectations that BHXB outbursts rise quickly and decay slowly (Chen, Shrader & Livio 1997).

## 6 DISCUSSION

We have presented a new, quasi-simultaneous broad-band spectrum covering the radio through X-ray wavebands for the BHXB J1357.2 in quiescence. Our data set includes the first UV constraints in quiescence, as well as the deepest radio observation to date (and to our knowledge, the deepest radio observation for any BHXB in quiescence that was known to be 'radio underluminous' in the hard state). The Eddington ratio during the observations was in the range $10^{-8.4} \lesssim L_X/L_{Edd} \lesssim 10^{-7.5}$, depending on the distance (2.3–6.3 kpc). The optical through X-ray fluxes are a factor of 2–5 times brighter during our observing campaign compared to previous epochs. However, no radio emission was detected in quiescence. It is unlikely that radio jet synchrotron emission is not detected simply because the proposed high-inclination nature of J1357.2 causes the jet to be beamed away from our line of sight. XTE J1118+480 is constrained to have a similar inclination as J1357.2 ($68^\circ < i < 79^\circ$ for XTE J1118+480; Khargharia et al. 2013), yet radio emission is detected from XTE J1118+480 at $L_X/L_{Edd} = 10^{-8.5}$ (Gallo et al. 2014). If J1357.2 launches a radio jet in quiescence, then the lack of a radio detection is either because J1357.2 is at too large of a distance to detect the radio jet, and/or because of intrinsic factors (e.g. lower bulk jet speeds, a jet axis that is not perpendicular to the orbital plane, etc.; see e.g. Gallo et al. 2014).

Armas Padilla et al. (2013) found that J1357.2 displayed a tight UV/X-ray luminosity correlation during its outburst decay (see Fig. 2), from which they determine that the UV radiation is dominated by a viscous accretion disc (also see Weng & Zhang 2015). Our observations show that the quiescent UV flux is almost two orders of magnitude fainter than the extrapolation of the UV/X-ray correlation to low X-ray fluxes, and the shape of the quiescent UV spectrum is also steeper. An outer UV accretion disc is likely present in quiescence (Hynes & Robinson 2012, also see e.g. McClintock et al. 2003; Froning et al. 2011, who detect broad UV emission lines in the quiescent UV spectra of both XTE J1118+480 and A0620−00). If the outer accretion disc were to account for all of the UV emission in quiescence, then the observed 'inversion' in UV colour between the hard state and quiescence would require a rapid decrease in the disc temperature, so that the UV probes the Rayleigh–Jeans tail in the hard state and the Wien tail in quiescence (the UV is very unlikely dominated by thermal emission from the companion star, given the companion's low stellar mass, the lack of observed orbital NIR/optical flux modulations, and the lack of stellar absorption features in the quiescent optical spectrum). While an outer disc almost certainly contributes some flux to the UV waveband, it cannot also explain the flat NIR spectrum in quiescence, and an extra emission component would be required. We argue below that, instead, synchrotron radiation provides a natural explanation for the entire SED, including the inversion in UV colour.

the 2010 January and 2010 July magnitudes follow similar distributions ($p = 0.1$ and 0.03 for the *WISE W1* and *W2* filters, respectively).

### 6.1 A synchrotron origin for quiescent BHXB emission

Plotkin et al. (2015) applied a broad-band spectral model to XTE J1118+480, which is the only other quiescent BHXB at an Eddington ratio comparable to J1357.2 that has a similarly rich, nearly simultaneous multiwavelength data set. Plotkin et al. (2015) conclude that the optical–UV spectrum of XTE J1118+480 arises from optically thin synchrotron radiation emitted by a mildly relativistic population of thermal electrons. These thermal electrons are associated with the jet base in the analysis of Plotkin et al. (2015, see Markoff, Nowak & Wilms 2005 for details). They also allow for a weakly accelerated, non-thermal tail of particles in the outer jet (at gravitational radii $r_g \gtrsim 10$–$10^2$) that attain maximum electron Lorentz factors $\gamma_{e,max} \lesssim 150$. This particle acceleration is too weak, however, for the non-thermal tail to contribute significant amounts of synchrotron radiation to the X-ray band. Therefore, in the above scenario for XTE J1118+480, the observed X-ray emission is synchrotron self-Compton (SSC) emitted by the same thermal electrons responsible for the synchrotron optical–UV emission. The same model applied to A0620−00 suggests a similar geometry for that source in quiescence as well (Gallo et al. 2007).

We attempted to apply the same broad-band model towards the SED of J1357.2 in quiescence. However, uncertainties on the distance, orbital inclination, and black hole mass leave too much degenerative parameter space to search through, preventing us from obtaining a fit with meaningful constraints. Instead, we phenomenologically interpret the broad-band spectrum below in order to highlight the most robust, model-independent results. We defer detailed broad-band modelling until the system parameters are better constrained.

Our conclusion for synchrotron-dominated optical/UV radiation that is emitted by a thermal population of electrons agrees with the conclusions of Shahbaz et al. (2013). Shahbaz et al. (2013) argue from a steep spectrum and short-term variability that synchrotron emission from thermal electrons dominates the optical emission from J1357.2 in quiescence. They similarly associate this thermal synchrotron emission with an outflowing jet instead of an inflowing RIAF: synchrotron radiation from the simplest class of RIAFs (i.e. the advection-dominated accretion flow, ADAF; e.g. Narayan & Yi 1994) is expected to display a sharp peak due to synchrotron self-absorption near $\nu_p \sim 10^{15}(M/\mathrm{M}_\odot)^{-1/2}$ Hz, which is not observed in the broad-band spectrum. We note that Shahbaz et al. (2013) analysed a non-simultaneous multiwavelength data set that did not contain radio, UV, and X-ray constraints. It is therefore possible for us to obtain a more complete picture of the quiescent jet from our quasi-simultaneous broad-band spectrum.

We expect the synchrotron jet emission to become optically thick at low frequencies. In other words, provided that multiple 'zones' along the jet contribute synchrotron radiation (with the peak temperature of the thermal electrons decreasing for zones farther from the black hole), the superposition of multiple synchrotron self-absorbed spectra will eventually create a flat spectrum at frequencies below a break frequency $\nu_b$ (where $\nu_b$ marks the optically thick transition; e.g. Blandford & Königl 1979). Extrapolating the NIR and optical spectra ($\alpha_{nir} = -0.1 \pm 0.1$ and $-1.2 \pm 0.3$; see Section 4.3) to higher and lower frequencies, respectively, we find that $\nu_b \approx (4.1 \pm 0.6) \times 10^{14}$ Hz. This calculation of $\nu_b$ neglects systematics due to variability, and the quoted (statistical) error is likely underestimated. Visual inspection of Fig. 4(b) indicates that $\nu_b$ must occur between the NIR $J$ and optical $r'$ filters. We therefore adopt a more conservative estimate of $\nu_b$ to be in the range $\approx$2–5 $\times 10^{14}$ Hz. We note that our radio limit constrains the outer jet to follow an optically thick, inverted spectrum with $\alpha_\nu > +0.3$ ($f_\nu \propto \nu^{\alpha_\nu}$) between the radio and IR/NIR wavebands, which further supports the idea of optically thick synchrotron radiation at low frequencies.

Shahbaz et al. (2013) concluded that the jet break should occur at $\nu_b < 2.5 \times 10^{13}$ Hz in their SED (at least an order of magnitude lower frequency than our constraint). Our 2014 jet break detection may therefore imply that $\nu_b$ varies with time, shifting through the IR and NIR bands. Rapid variability of $\nu_b$ through the IR has also been observed for GX 339−4 in the hard state, which is most likely caused by fast variations in the strength of the jet magnetic field (Gandhi et al. 2011). We note that the Shahbaz et al. (2013) NIR data points from 2013 March also appear to follow a flat spectrum in Fig. 4(b), which further supports a variable jet break frequency (the rest of the multiwavelength data that their $\nu_b < 2.5 \times 10^{13}$ Hz limit is based on was obtained 1–3 yr prior to their 2013 NIR observations).

If the approximately flat NIR spectrum is due to an optically thick jet,[7] then this would mark the first time that an optically thick-to-thin jet break has been directly observed in quiescence (emission from the companion stars in A0620−00 and XTE J1118+480 prohibit jet break identifications in those systems without broad-band spectral modelling). Jet breaks have been isolated in almost a dozen hard state systems (e.g. Corbel et al. 2002; Russell et al. 2013). However, we caution that drawing a physical connection between a jet break for J1357.2 in quiescence and for the hard state systems is currently premature, as the jet breaks that have been isolated in hard state systems are intimately related to the location along the jet where (some fraction of) particles are accelerated into non-thermal distributions (e.g. Polko, Meier & Markoff 2013, 2014). For J1357.2 it is unclear if such an acceleration zone exists in quiescence, and the potential jet break may rather simply represent the optically thick to thin transition of a multizone jet composed purely of a thermal distribution of particles.

#### 6.1.1 *X-ray radiation mechanisms in quiescence*

Interpretation of the X-ray emission highly depends on the efficiency of particle acceleration along the jet (i.e. the maximum Lorentz factor, $\gamma_{e,max}$, attained by accelerated particles). If particle acceleration is weak (with $\gamma_{e,max} < 10^2$, as suggested by Plotkin et al. 2015 for XTE J1118+480), then (non-thermal) synchrotron radiation from the jet will quickly cool and not contribute significantly at X-ray energies. The optical–UV spectrum would be synchrotron radiation from thermal electrons as described above, and the X-rays must be corresponding (thermal) SSC.

If particle acceleration is instead efficient (i.e. $\gamma_{e,max} > 10^2$), then synchrotron emission from non-thermal electrons (and/or corresponding SSC) along the accelerated jet would be responsible for most of the observed X-rays. However, the (steep) *Chandra* X-ray spectrum implies that any non-thermal electrons must suffer from radiative losses, and the X-rays would be synchrotron cooled.[8] In that case, the slope of the radio/X-ray correlation would steepen by

[7] It is also a possibility that the flat NIR spectrum could rather be associated with an entirely optically thin synchrotron component (emitted by the thermal jet) that simply peaks near the NIR.

[8] Electrons injected into a non-thermal distribution by e.g. diffusive shock acceleration processes will follow a particle spectrum $n_e(\gamma_e) \propto \gamma_e^{-p}$, where $n_e$ is the electron density, $\gamma_e$ is the Lorentz factor of each electron, and the spectral slope $p$ is typically 2–2.4. Radiative cooling losses will modify the spectral slope to steepen by $p + 1$ at X-ray energies, yielding an X-ray photon index for synchrotron cooled jet emission of $\Gamma = (p + 2)/2 \approx 2$.

a factor of ≈2 in quiescence (Yuan & Cui 2005), and the corresponding optically thick synchrotron radio emission from the outer jet would be well below the sensitivity of our VLA observations.

Either efficient or inefficient particle acceleration along the jet is consistent with the observed X-ray spectrum. However, in both scenarios, the NIR–UV emission must always be dominated by synchrotron radiation from *thermal* electrons. To illustrate this point, it is clear from Fig. 3 that the UV emission follows a steeper spectral slope than the X-ray emission. The UV emission therefore cannot also be synchrotron cooled radiation from the same non-thermal electrons (or else the UV and X-ray radiation would follow similar spectral slopes). In order for X-rays to be emitted by synchrotron cooled radiation, the synchrotron cooling break must fall below the X-ray waveband (i.e. $\nu_{\rm cool} \lesssim 10^{17}$ Hz). At frequencies below the cooling break, synchrotron radiation from accelerated non-thermal electrons would be optically thin (i.e. the spectrum would become *flatter*, with a photon index smaller by $\Delta\Gamma = 0.5$; e.g. Rybicki & Lightman 1979). To explain the observed shape (and especially curvature) of the optical/UV spectrum, the thermal synchrotron component must dominate over any optically thin synchrotron radiation emitted by the accelerated particles. *Thus, regardless of the particle acceleration efficiency and the mechanism that produces the X-ray radiation, emission from a thermal (relativistic) population of electrons always dominates the lower energy radiation.*

## 7 CONCLUSIONS

From a new quasi-simultaneous SED of J1357.2 in quiescence, we obtain the following.

(i) We isolate the frequency where the jet transitions from optically thick-to-thin to be $\nu_{\rm b} \approx 2$–$5 \times 10^{14}$ Hz, which represents the first direct detection of a jet break in a quiescent BHXB. Comparing to the $\nu_{\rm b} < 2.5 \times 10^{13}$ Hz limit placed by Shahbaz et al. (2013) at earlier epochs, our detection suggests a variable jet break frequency in quiescence that shifts through the IR/NIR bands.

(ii) Nearly simultaneous UV and X-ray observations show a switch in the UV radiation mechanism in quiescence compared to the hard state. This result is consistent with a thermal synchrotron 'bump' peaking near the optical (akin to the 'sub-mm bump' in Sgr A*; e.g. Serabyn et al. 1997; Falcke & Markoff 2000), which could be a common feature of quiescent, short-period low-mass BHXBs (such a feature is also seen for XTE J1118+480 and A0620−00 in quiescence). We demonstrate that the thermal synchrotron origin of this component does not depend on the details of the X-ray emission mechanism.

(iii) We provided the deepest radio limit yet for any BHXB in quiescence that was known to be 'radio underluminous' in the hard state. This limit indicates that the outer (quiescent) jet follows an inverted, optically thick synchrotron spectrum ($\alpha_\nu > 0.3$).

Finally, we conclude by noting that our UV constraints were crucial for reaching many of our conclusions (especially the second bullet point above). Without the UV constraints on the curvature of the optical–UV spectrum, it would be tempting to connect the optical and X-ray emission with a simple (synchrotron cooled) power law, while attributing the difference between optical and X-ray flux normalizations to day-long variability between the two wavebands. High Galactic latitude sources are therefore critical for opening the UV window and understanding very low Eddington ratio accretion flows (also see McClintock et al. 2003). This key point should serve as further motivation for black hole surveys targeting high Galactic latitudes.

## ACKNOWLEDGEMENTS

We thank the anonymous referee for insightful comments that improved this paper. We greatly appreciate the efforts of the CXC and NRAO schedulers for coordinating the simultaneous *Chandra* and VLA observations. We also thank Neil Gehrels and the *Swift* team for approving and scheduling the *Swift*/UVOT observations. We thank Adam Kowalski for helpful discussions regarding M-stars, and Edmund Hodges-Kluck for advice related to *Swift*/UVOT. Support for this work was provided by the National Aeronautics and Space Administration through *Chandra* Award Number GO4-15042X issued by the *Chandra* X-ray Observatory Center, which is operated by the Smithsonian Astrophysical Observatory for and on behalf of the National Aeronautics Space Administration under contract NAS8-03060. JCAM-J is the recipient of an Australian Research Council Future Fellowship (FT140101082). TM-D acknowledges support by the Spanish Ministerio de Economa y competitividad (MINECO) under grant AYA2013-42627. This research has made use of software provided by the *Chandra* X-ray Center (CXC) in the application package CIAO. The William Herschel Telescope is operated on the island of La Palma by the Isaac Newton Group in the Spanish Observatorio del Roque de los Muchachos of the Instituto de Astrofsica de Canarias. The National Radio Astronomy Observatory is a facility of the National Science Foundation operated under cooperative agreement by Associated Universities, Inc. This publication makes use of data products from the *Wide-field Infrared Survey Explorer*, which is a joint project of the University of California, Los Angeles, and the Jet Propulsion Laboratory/California Institute of Technology, funded by the National Aeronautics and Space Administration.

## REFERENCES

Abramowicz M. A., Chen X., Kato S., Lasota J.-P., Regev O., 1995, ApJ, 438, L37
Armas Padilla M., Degenaar N., Russell D. M., Wijnands R., 2013, MNRAS, 428, 3083
Armas Padilla M., Wijnands R., Altamirano D., Méndez M., Miller J. M., Degenaar N., 2014a, MNRAS, 439, 3908
Armas Padilla M., Wijnands R., Degenaar N., Muñoz-Darias T., Casares J., Fender R. P., 2014b, MNRAS, 444, 902
Bernardini F., Cackett E. M., 2014, MNRAS, 439, 2771
Blandford R. D., Begelman M. C., 1999, MNRAS, 303, L1
Blandford R. D., Königl A., 1979, ApJ, 232, 34
Brocksopp C., Corbel S., Fender R. P., Rupen M., Sault R., Tingay S. J., Hannikainen D., O'Brien K., 2005, MNRAS, 356, 125
Cadolle Bel M. et al., 2007, ApJ, 659, 549
Calvelo D. E. et al., 2010, MNRAS, 409, 839
Cao X.-F., Wu Q., Dong A.-J., 2014, ApJ, 788, 52
Cash W., 1979, ApJ, 228, 939
Chen W., Shrader C. R., Livio M., 1997, ApJ, 491, 312
Corbel S., Fender R. P., Tzioumis A. K., Tomsick J. A., Orosz J. A., Miller J. M., Wijnands R., Kaaret P., 2002, Science, 298, 196
Corbel S., Fender R. P., Tomsick J. A., Tzioumis A. K., Tingay S., 2004, ApJ, 617, 1272
Corbel S., Coriat M., Brocksopp C., Tzioumis A. K., Fender R. P., Tomsick J. A., Buxton M. M., Bailyn C. D., 2013, MNRAS, 428, 2500
Coriat M. et al., 2011, MNRAS, 414, 677
Corral-Santana J. M., Casares J., Muñoz-Darias T., Rodríguez-Gil P., Shahbaz T., Torres M. A. P., Zurita C., Tyndall A. A., 2013, Science, 339, 1048
Dzib S. A., Massi M., Jaron F., 2015, A&A, 580, L6
Falcke H., Markoff S., 2000, A&A, 362, 113
Feigelson E. D., Nelson P. I., 1985, ApJ, 293, 192
Fender R. P., 2001, MNRAS, 322, 31

Froning C. S. et al., 2011, ApJ, 743, 26
Fruscione A. et al., 2006, Proc. SPIE, 6270, 62701V
Gallo E., Fender R., Corbel S., 2003, Astron. Telegram, 196, 1
Gallo E., Fender R. P., Hynes R. I., 2005, MNRAS, 356, 1017
Gallo E., Fender R. P., Miller-Jones J. C. A., Merloni A., Jonker P. G., Heinz S., Maccarone T. J., van der Klis M., 2006, MNRAS, 370, 1351
Gallo E., Migliari S., Markoff S., Tomsick J. A., Bailyn C. D., Berta S., Fender R., Miller-Jones J. C. A., 2007, ApJ, 670, 600
Gallo E., Miller B. P., Fender R., 2012, MNRAS, 423, 590
Gallo E. et al., 2014, MNRAS, 445, 290
Gandhi P. et al., 2011, ApJ, 740, L13
Garmire G. P., Bautz M. W., Ford P. G., Nousek J. A., Ricker G. R., Jr, 2003, Proc. SPIE, 4851, 28
Heinz S., Sunyaev R. A., 2003, MNRAS, 343, L59
Hjellming R. M., Johnston K. J., 1988, ApJ, 328, 600
Hjellming R. M., Rupen M. P., Mioduszewski A. J., Narayan R., 2000, Astron. Telegram, 54, 1
Houck J. C., Denicola L. A., 2000, in Manset N., Veillet C., Crabtree D., eds, ASP Conf. Ser. Vol. 216, Astronomical Data Analysis Software and Systems IX. Astron. Soc. Pac., San Francisco, p. 591
Hynes R. I., Robinson E. L., 2012, ApJ, 749, 3
Hynes R. I. et al., 2004, ApJ, 611, L125
Hynes R. I., Bradley C. K., Rupen M., Gallo E., Fender R. P., Casares J., Zurita C., 2009, MNRAS, 399, 2239
Ichimaru S., 1977, ApJ, 214, 840
Jonker P. G., Gallo E., Dhawan V., Rupen M., Fender R. P., Dubus G., 2004, MNRAS, 351, 1359
Jonker P. G. et al., 2010, MNRAS, 401, 1255
Jonker P. G., Miller-Jones J. C. A., Homan J., Tomsick J., Fender R. P., Kaaret P., Markoff S., Gallo E., 2012, MNRAS, 423, 3308
Kataoka J. et al., 2008, ApJ, 672, 787
Khargharia J., Froning C. S., Robinson E. L., Gelino D. M., 2013, AJ, 145, 21
Krimm H. A. et al., 2011a, Astron. Telegram, 3138, 1
Krimm H. A., Kennea J. A., Holland S. T., 2011b, Astron. Telegram, 3142, 1
Lavalley M., Isobe T., Feigelson E., 1992, in Worrall D. M., Biemesderfer C., Barnes J., eds, ASP Conf. Ser. Vol. 25, Astronomical Data Analysis Software and Systems I. Astron. Soc. Pac., San Francisco, p. 245
McClintock J. E., Narayan R., Garcia M. R., Orosz J. A., Remillard R. A., Murray S. S., 2003, ApJ, 593, 435
McMullin J. P., Waters B., Schiebel D., Young W., Golap K., 2007, in Shaw R. A., Hill F., Bell D. J., eds, ASP Conf. Ser. Vol. 376, Astronomical Data Analysis Software and Systems XVI. Astron. Soc. Pac., San Francisco, p. 127
Markoff S., Falcke H., Fender R., 2001, A&A, 372, L25
Markoff S., Nowak M., Corbel S., Fender R., Falcke H., 2003, A&A, 397, 645
Markoff S., Nowak M. A., Wilms J., 2005, ApJ, 635, 1203
Markoff S. et al., 2015, ApJ, 812, L25
Markwardt C. B., 2009, in Bohlender D. A., Durand D., Dowler P., eds, ASP Conf. Ser. Vol. 411, Astronomical Data Analysis Software and Systems XVIII. Astron. Soc. Pac., San Francisco, p. 251
Mata Sánchez D., Muñoz-Darias T., Casares J., Corral-Santana J. M., Shahbaz T., 2015, MNRAS, 454, 2199
Meyer-Hofmeister E., Meyer F., 2014, A&A, 562, A142
Miller J. M. et al., 2006, ApJ, 646, 394
Miller-Jones J. C. A., Jonker P. G., Maccarone T. J., Nelemans G., Calvelo D. E., 2011, ApJ, 739, L18
Munar-Adrover P., Paredes J. M., Ribó M., Iwasawa K., Zabalza V., Casares J., 2014, ApJ, 786, L11
Narayan R., Yi I., 1994, ApJ, 428, L13
Narayan R., Igumenshchev I. V., Abramowicz M. A., 2000, ApJ, 539, 798
Perley R. A., Butler B. J., 2013, ApJS, 204, 19
Plotkin R. M., Markoff S., Kelly B. C., Körding E., Anderson S. F., 2012, MNRAS, 419, 267
Plotkin R. M., Gallo E., Jonker P. G., 2013, ApJ, 773, 59
Plotkin R. M., Gallo E., Markoff S., Homan J., Jonker P. G., Miller-Jones J. C. A., Russell D. M., Drappeau S., 2015, MNRAS, 446, 4098
Polko P., Meier D. L., Markoff S., 2013, MNRAS, 428, 587
Polko P., Meier D. L., Markoff S., 2014, MNRAS, 438, 959
Quataert E., Gruzinov A., 2000, ApJ, 539, 809
Ratti E. M. et al., 2012, MNRAS, 423, 2656
Rau A., Greiner J., Filgas R., 2011, Astron. Telegram, 3140, 1
Reis R. C., Fabian A. C., Miller J. M., 2010, MNRAS, 402, 836
Remillard R. A., McClintock J. E., 2006, ARA&A, 44, 49
Reynolds M. T., Reis R. C., Miller J. M., Cackett E. M., Degenaar N., 2014, MNRAS, 441, 3656
Rodriguez J., Cadolle Bel M., Tomsick J. A., Corbel S., Brocksopp C., Paizis A., Shaw S. E., Bodaghee A., 2007, ApJ, 655, L97
Roming P. W. A. et al., 2005, Space Sci. Rev., 120, 95
Russell D. M., Maitra D., Dunn R. J. H., Markoff S., 2010, MNRAS, 405, 1759
Russell D. M. et al., 2013, MNRAS, 429, 815
Rybicki G. B., Lightman A. P., 1979, Radiative Processes in Astrophysics. Wiley-Interscience, New York
Schirmer M., 2013, ApJS, 209, 21
Serabyn E., Carlstrom J., Lay O., Lis D. C., Hunter T. R., Lacy J. H., Hills R. E., 1997, ApJ, 490, L77
Shahbaz T., Russell D. M., Zurita C., Casares J., Corral-Santana J. M., Dhillon V. S., Marsh T. R., 2013, MNRAS, 434, 2696
Sivakoff G. R., Miller-Jones J. C. A., Krimm H. A., 2011, Astron. Telegram, 3147, 1
Skrutskie M. F. et al., 2006, AJ, 131, 1163
Soleri P., Fender R., 2011, MNRAS, 413, 2269
Steele I. A. et al., 2004, Proc. SPIE, 5489, 679
Torres M. A. P., Jonker P. G., Miller-Jones J. C. A., Steeghs D., Repetto S., Wu J., 2015, MNRAS, 450, 4292
Weng S.-S., Zhang S.-N., 2015, MNRAS, 447, 486
Wright E. L. et al., 2010, AJ, 140, 1868
Xue Y. Q., Cui W., 2007, A&A, 466, 1053
Yuan F., Cui W., 2005, ApJ, 629, 408
Yuan F., Cui W., Narayan R., 2005, ApJ, 620, 905

This paper has been typeset from a TEX/LATEX file prepared by the author.